RESEARCH ARTICLES

Solar Wind Origin in Coronal Funnels

Chuan-Yi Tu,[1,3]* Cheng Zhou,[2] Eckart Marsch,[3] Li-Dong Xia,[4] Liang Zhao,[1] Jing-Xiu Wang,[5] Klaus Wilhelm[3]

The origin of the solar wind in solar coronal holes has long been unclear. We establish that the solar wind starts flowing out of the corona at heights above the photosphere between 5 megameters and 20 megameters in magnetic funnels. This result is obtained by a correlation of the Doppler-velocity and radiance maps of spectral lines emitted by various ions with the force-free magnetic field as extrapolated from photospheric magnetograms to different altitudes. Specifically, we find that Ne^{7+} ions mostly radiate around 20 megameters, where they have outflow speeds of about 10 kilometers per second, whereas C^{3+} ions with no average flow speed mainly radiate around 5 megameters. Based on these results, a model for understanding the solar wind origin is suggested.

The solar wind has been an essential topic in space physics ever since 1951 when it was inferred from cometary observations (1) and predicted from coronal models (2). Its properties were then analyzed through in situ observations (3, 4). However, even after five decades of spacecraft exploration and theoretical modeling, the exact source of the solar wind in the solar atmosphere remains a mystery.

In the 1960s and 1970s, the "coronal base" (5–10) was assumed to be the inner boundary of the solar wind, yet its location and properties remained poorly defined. Considering that heating of the corona and acceleration of the solar wind are closely related, the models were extended throughout the solar transition region (TR) down to the chromosphere (11–13). It was suggested that the place where hydrogen becomes ionized might be considered as the inner boundary (14). In the past decade, models were developed with the assumption that the solar wind is created in coronal funnels (15–18), which are magnetic structures expanding into the corona with a narrow neck in the photosphere (19, 20).

For observations and diagnostics of the solar wind source, the spectrometer SUMER (Solar Ultraviolet Measurements of Emitted Radiation) on SOHO (Solar and Heliospheric Observatory) provides a variety of spectral lines emitted in the chromosphere, transition region, or corona (21, 22). However, solar disk observa- tions resolved only two-dimensional (2-D) structures seen in planar projection and provided no height information along the line of sight (LOS). Hassler et al. (23) and Wilhelm et al. (24) identified the source regions of the fast solar wind by means of radiance and Doppler-shift maps in the polar coronal hole (CH), and Xia et al. (25, 26) in equatorial CHs. The key tool for detecting outflow was the Doppler blueshift (indicating negative LOS velocities of the plasma away from the solar surface) of the emission line of Ne^{7+} at 77 nm. In these studies, the Ne VIII emission was compared with the Si II radiance in projected 2-D maps. However, the altitude of the emission regions remained unclear, as did the location where the solar wind acceleration actually starts.

Limb observations can reveal the height variation of the emission, but even then different structures are mixed together along the LOS. Moreover, they are perpendicular to the radial direction and therefore do not allow one to study radial outflow with the help of line-shift measurements. Although the coronal magnetic field cannot be measured directly, it can be constructed by various extrapolation methods (27) and so may provide some height information.

Only recently have magnetic fields, measured as photospheric magnetograms by MDI (Michelson Doppler Imager) (28) or Earth-based solar observatories, been used to determine the 3-D coronal field at low altitudes and spatial scales down to 1 Mm. The fields in active regions (AR) and CHs were constructed by force-free extrapolation from MDI data (29). The extrapolation technique is applied in a finite rectangular segment of the solar atmosphere and provides the coronal magnetic field $\mathbf{B}(x, y, z)$, with Cartesian components B_x, B_y, and B_z, where z is the vertical component, and x and y are the horizontal components, of the radial distance vector $\mathbf{r}$.

The model field has not yet been correlated at various heights with the ultraviolet emission patterns, especially in CHs where no bright loops occur. Such correlations are presented here to answer two important questions: At which height in CHs is the coronal base located, and where in coronal funnels does the solar wind flow start? We obtain the formation heights of spectral lines from a correlation of their radiances and Doppler maps with the extrapolated magnetic field and find that the acceleration starts between 5 Mm and 20 Mm above the photosphere and that speeds of about 10 km/s may be reached at 20 Mm.

Therefore, the inner boundary of the solar wind is neither at the old coronal base nor at the top of the chromosphere but should be defined as the point in the funnel where downflow changes into outflow, implying also sideflows consistent with supergranular convection. These results contrast with conventional (1-D) solar wind models (30), in which plasma starts flowing from about 2 Mm, whereby it is assumed that mass, momentum, and energy are conserved along the magnetic flux tube linking the upper chromosphere with the lower corona. The results obtained here shed new light on the magnetic structure and location of the solar wind source.

Correlations between radiation and magnetic field. We use data from the emission lines Si II (153.3 nm), C IV (154.8 nm), and Ne VIII (77.0 nm) measured by SUMER. These ultraviolet lines are emitted by the following ions: (i) Si^+, formed at an electron temperature of about 2×10^4 K in the chromosphere; (ii) C^{3+}, formed at 1×10^5 K in the TR, and (iii) Ne^{7+}, formed at 6×10^5 K in the lower corona. The observations were made in the polar CH on 21 September 1996 from 00:15 to 07:30 UTC. The region studied is shown in Fig. 1A as a large rectangle superimposed on the Fe XII image of EIT (Extreme-Ultraviolet Imaging Telescope) (31). To compare the magnetic field with the SUMER images, we used the MDI magnetograms for the field extrapolation over an area of 384″ by 231″, which is a little bigger than the small rectangle (of size 311″ by 201″′) in Fig. 1A. For details on data analysis, see (32).

Figure 1B shows a map of B_z, which is obtained by correcting the MDI data for the LOS effect, that is, by dividing through by $\cos 55° = 0.57$, appropriate for the average latitude. Figure 1, C to E, shows the Si II and C IV radiances and Ne VIII Doppler shift. Hassler et al. (23) found a relation between the Ne VIII Doppler shift and the chromospheric network, as inferred by visual inspection of the Si II radiance patterns, in the sense that the strongest outflow was observed near network lanes and their intersections. How-

[1]Department of Geophysics, Peking University, Beijing 100871, China. [2]Department of Atmospheric Sciences, Peking University, Beijing 100871, China. [3]Max-Planck-Institut für Sonnensystemforschung, 37191 Katlenburg-Lindau, Germany. [4]School of Earth and Space Sciences, University of Science and Technology of China, Hefei, Anhui 230026, China. [5]National Astronomical Observatories, Chinese Academy of Sciences, Beijing 100012, China.

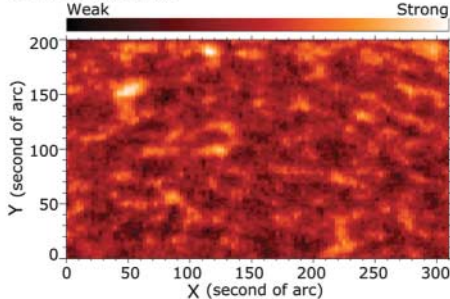*To whom correspondence should be addressed. E-mail: cytu@public3.bta.net.cn
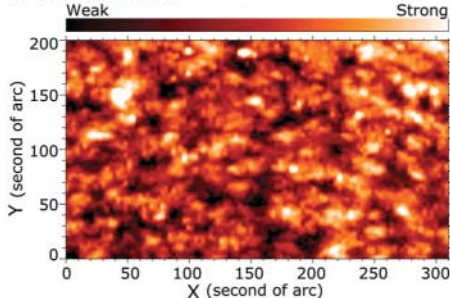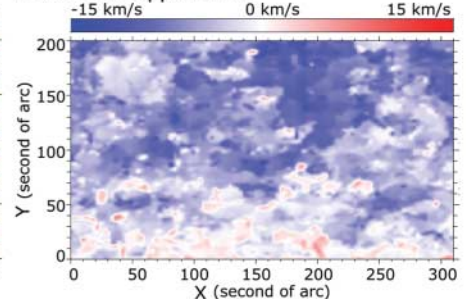
A EIT 19.5 nm
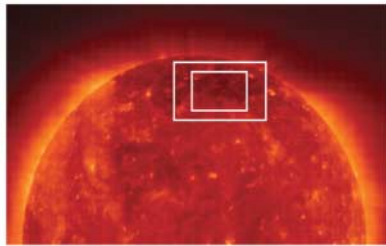
B Magnetic field
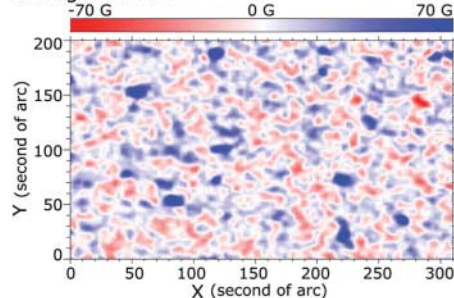
C Si II Radiance

D C IV Radiance

E Ne VIII Doppler shift
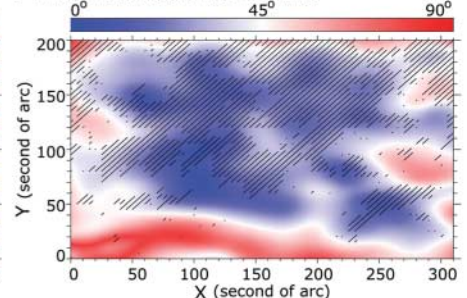

F Field inclination at 20.6 Mm

Fig. 1. (**A**) The Sun in the wavelength window around 19.5 nm. The large white rectangle indicates the original size of the SUMER raster scan. A comparison of the structures was made only for the smaller rectangle. (**B**) Magnetic field vertical component ranging from −70 G to 70 G. (**C**) Si II radiance and (**D**) C IV radiance, both in arbitrary units. (**E**) Ne VIII Doppler shifts along the LOS, ranging from −15 km/s to 15 km/s. (**F**) Comparison between the Ne VIII Doppler shift (hatched regions with outflow speeds higher than 7 km/s) and the magnetic field angle, with 0° indicating vertical and 90° horizontal orientations at the height z = 20.6 Mm.

ever, according to Fig. 1, C and E, there is no clear overall correlation, mainly because the structures in the Ne VIII Doppler map are larger than those in the Si II radiance map.

Clearly, the Ne VIII and Si II lines are not emitted at the same height. To determine these heights, we used the method of Seehafer (*33*), as Marsch *et al.* did for ARs [(*29*), equations 1 to 3 for B_x, B_y, and B_z], and extrapolated in a force-free way the photospheric magnetic field to the TR and corona. In the extrapolation box, the positive x coordinate is westward, the y coordinate northward in the tangent plane, and z upward. We considered foreshortening by dividing the apparent distance in the y direction through cos55°. Then we calculated the correlations between radiance maps and 2-D charts of the coronal B_z at different heights.

The result is shown in Fig. 2A. The number of data points for each plot is 62,511. The critical value of 0.008 for the linear correlation coefficient is determined with 95% confidence. The correlation coefficient between the Ne VIII blueshift and $|B_z/B|$ clearly increases with growing z and reaches a maximum of 0.39 at 20.6 Mm. For Si II, it reaches a maximum value of 0.50 at 4.0 Mm and for C IV, 0.18 at 4.5 Mm. The horizontal bar shows the z range in which the coefficient is above 95% of its maximum. The heights of maximal correlation for Si, C, and Ne range from 1.5 to 7.0, 2.0 to 7.0, and 16 to 29 Mm, respectively. For disk observations, the correlation technique is perhaps
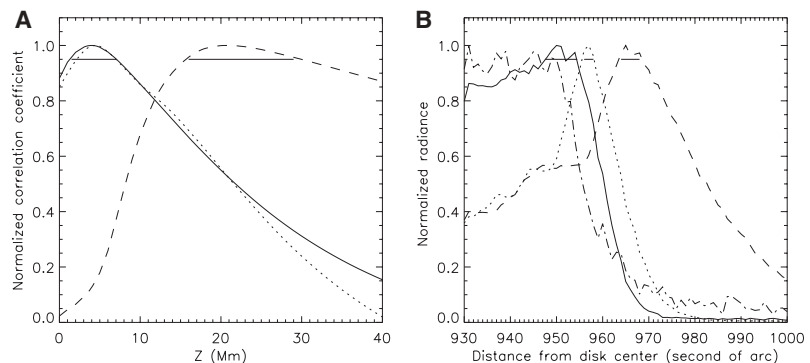

Fig. 2. (**A**) Height variations of the correlation coefficients. The solid line gives the coefficient (normalized by 0.50) between line radiance and $|B_z|$ for Si II, the dotted line the coefficient (normalized by 0.18) for C IV. The dashed line gives the coefficient (normalized by 0.39) between the Ne VIII blueshift and $|B_z/B|$. (**B**) Radial variations of the line radiances of Si II, C IV and Ne VIII, and of the continuum at 154.31 nm, which is indicated by the dash-dot line. The solid line indicates Si II, the dotted C IV, and the dashed Ne VIII. All radiances are normalized to their maximum values. The data were taken across the limb, within the upper right corner of the larger rectangle in Fig. 1A. To indicate the precision by which one can determine the maximum height, we have drawn horizontal bars extending between the two locations where the coefficients drop below 95% of the maximum.

the only quantitative method to determine emission heights. We are convinced that our results are reliable for the following reasons:

(i) Our disk results are consistent with off-limb observations. Figure 2B shows the radial variations of the Si II, C IV, and Ne VIII radiances, with data from the upper right corner of the large rectangle in Fig. 1A. The difference between the maxima of the Si II and Ne VIII profiles is 15″ or 11 Mm (a view angle of 1″ corresponds to a distance of 721 km at the Sun), whereas between the correlation heights it is 16 Mm. Considering the uncer-

tainties of both methods, the results can be considered as consistent.

(ii) Figure 3A shows the Ne VIII Doppler shift versus $|B_z/B|$ at 20.6 Mm. The 31,321 data points were selected under the condition $|B_y/B_x| < 1$ to ensure that the vertical field has a component along the LOS. For a nearly horizontal field, the flow speed is about zero. In contrast, outflows are concentrated at locations of nearly vertical fields. This can be seen in Fig. 1F, which shows a comparison between Ne VIII Doppler shift and field inclination. Figure 3B displays the square

Fig. 3. Results from the linear correlation analyses. The asterisks indicate the average values in vertical bins, with one SD. The fit parameters are given in Table 1. (**A**) Plot of the Ne VIII Doppler shift versus $|B_z/B|$ at 20.6 Mm. (**B**) Plot of the square root of the Si II radiance versus $|B_z|$ at 4.0 Mm.
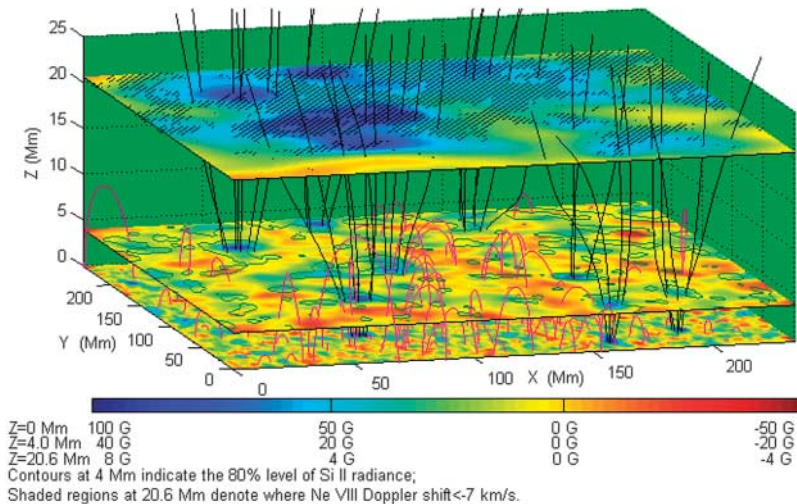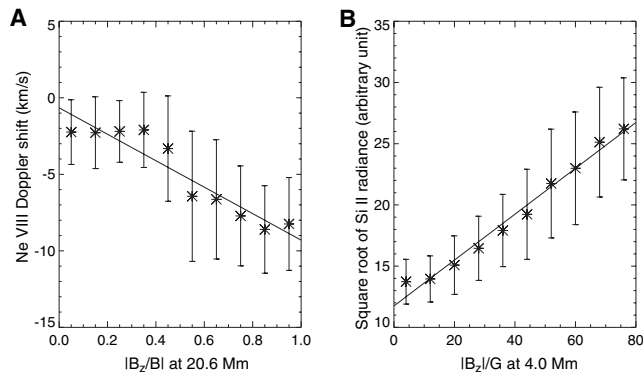

Fig. 4. Magnetic field structures in the 3-D solar atmosphere. The black solid curves illustrate open and the red curves closed field lines. Because the magnetic field strength decreases with increasing height (Z) in the corona, the scales on the color bars differ for different Z. In the plane inserted at 4 Mm, we compare the Si II radiance with the extrapolated B_z. The contours delineate the 80% level of the Si II radiance. In the plane inserted at 20.6 Mm, we compare the Ne VIII Doppler shifts smaller than −7 km/s with the extrapolated B_z. The shaded areas indicate where the Ne^{7+} outflow speed is larger than 7 km/s.

thermal pressure balances the magnetic pressure. In our model without any current sheets, a unipolar funnel is surrounded by bipolar loops controlling the funnel shape.

The linear force-free field extrapolation may be a good approximation for the TR if the underlying photospheric area is large enough and if no data near the boundaries are used. Our area is 277 Mm by 292 Mm. We considered extrapolation up to 40 Mm and did not use data near boundaries (~27 Mm on each side in the x direction and 11 Mm on each side in the y direction). Short-term magnetic activities such as micro- and nanoflares, or field topology changes and magnetic reconnection can of course not be described by the force-free model.

Outflow pattern and funnel shape. As illustrated in Fig. 3, the Ne^{7+} outflow pattern is closely correlated with the magnetic field inclination $|B_z/B|$. Figure 4 shows a strong correlation with B_z itself. A large B_z and vertical fields represent open coronal funnels, being rooted in strong photospheric fields. Figure 4 shows the field strength at $z = 0$ Mm, $z = 4$ Mm, and $z = 20.6$ Mm, together with Si II radiance contours (top 80%) at $z = 4$ Mm and Ne VIII Doppler shifts at $z = 20.6$ Mm. The field line spreading and associated blue patches indicate the expansion of the funnels. Obviously, the Ne^{7+} outflow is controlled and guided by the funnel shape at 20.6 Mm. The funnels are rooted near supergranulation boundaries in the network lanes.

Where in the funnel does the solar wind acceleration actually start? To answer this question in comparison with models, we identified a single funnel linking the TR with the corona and correlated the observed radiances and Doppler shifts with the extrapolated magnetic fields. Gabriel (*19*) presented his seminal funnel model for a unipolar field region. Dowdy *et al.* (*20*) discussed a static conceptual model for the 3-D geometry of the TR, including multiple loops between open funnels. Other authors (*15*, *17*, *18*) developed various dynamical funnel models based on 1-D fluid equations, including waves and plasma flow.

The extrapolated field in Fig. 4 shows many closed loops between the funnels in this CH region. Some of the loops reach as high as 7 Mm. The funnel rooted at $x = 110$ Mm and $y = 150$ Mm merges with two others, thus forming a large strong-field region. It coincides with the hatched patches, which indicates a comparatively high outflow speed there. Further details of the field geometry around this funnel are shown in Fig. 5A. We only illustrate some open field lines and surrounding closed loops, which seem to quench the funnel.

Figure 5B again shows this funnel, which does not have a canopy shape as originally suggested (*19*). Its cross section increases almost linearly with height, leading to 12 times its photospheric area at 21 Mm. Concurrently, the field strength decreases from 63.9 G

root of the Si II radiance, which is proportional to the electron density, versus the absolute value of B_z at 4.0 Mm. The 39,117 data points were selected under the constraint $|B_z/B| > 0.5$ to ensure that the extrapolated field is vertical. The correlations shown in Fig. 3, A and B, are high. This indicates that the extrapolated field is reasonable and its morphology consistent with the radiance pattern.

(iii) The correlation height hardly changes with α, which has the dimension of an inverse length, the gradient scale of the field. We considered two situations: $\alpha = -1.1 \times 10^{-8}$ m^{-1}, which is the value derived for the force-free field in an AR (*29*); and $\alpha = 0$ for a potential field. Theoretically, steady open flux tubes should have no twist, that is, $\alpha = 0$, because twists will become Alfvén waves escaping from the funnel. We obtained similar correlation heights for both values of α. We confirmed that the field extrapolation in CHs does not critically depend on α up to 40 Mm. The mean heights (variance given in parentheses) of maximum correlation (for $\alpha = 0$) are Si II

$z = 4.0$ Mm (1.3–7.1), C IV $z = 5.0$ Mm (2.7–7.5), and Ne VIII $z = 24$ Mm (17.5–33).

(iv) The conditions prevailing in the CH regions fulfill the requirements for a stationary, force-free field extrapolation. Structures in the solar atmosphere such as supergranulation, chromospheric network, and magnetic funnels all are comparatively long-lived (tens of hours), and thus their time variations do not matter. The SUMER data are taken within several hours.

The force-free assumption appears reasonable, considering that the vertical gradient of the thermal pressure balances the gravity force and that the magnetic pressure dominates the thermal pressure. Because the unipolar funnel is surrounded by strong bipolar fields reaching up to about 7 Mm (Fig. 4, lower level), the adjacent loops keep the funnel's cross section constricted, and thus through magnetic tension prevent a rapid horizontal expansion of the funnel with height. This is different from the classical Gabriel model (*19*), in which a horizontal current sheet exists at the bottom of the funnel at 1500 km, where the

Fig. 5. Magnetic funnel in the solar atmosphere. (**A**) Emphasis on open field lines and correlation with the Ne^{7+} outflow speed larger than 8 km/s (dark shading). (**B**) Illustration of the funnel boundary and magnetic unipolar flux constriction by adjacent, surrounding bipolar loops.
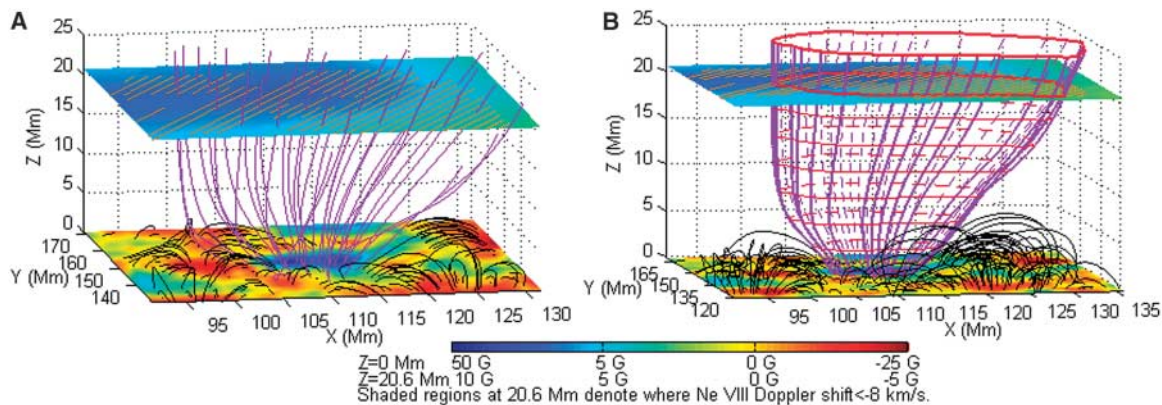

Z=0 Mm   50 G   5 G   0 G   -25 G
Z=20.6 Mm 10 G   0 G   0 G   -5 G
Shaded regions at 20.6 Mm denote where Ne VIII Doppler shift<-8 km/s.

Table 1. Parameters of the linear correlation analysis with 10 magnetic field data bins.

Parameter	Coefficient	$|B_z|/10$ G	$|B_z/B|$
Si II Radiance (arbitrary unit)	R	0.99	0.96
	a	11.75 ± 0.41	13.29 ± 0.09
	b	1.87 ± 0.09	1.53 ± 0.16
C IV Doppler shift (km/s)	R	0.91	0.92
	a	−0.97 ± 0.11	−0.99 ± 0.08
	b	+0.60 ± 0.10	+0.95 ± 0.15
Ne VIII Doppler shift (km/s)	R	−0.76	−0.94
	a	−3.33 ± 1.09	−0.66 ± 0.64
	b	−8.87 ± 2.67	−8.64 ± 1.11

(6.39 mT) in the photosphere to 5.3 G at 21 Mm. How fast a funnel can diverge is determined by the surrounding loops, which push laterally on the funnel. This result agrees with the sketch of intermingling funnels and loops as drawn by Dowdy *et al.* (*20*) and suggested by Peter (*34, 35*) and supports the idea that "the funnels are constricted at their base in the network not only by the supergranular flow but also by crowding from the ambient magnetic field of the many closed loops" (*20*).

Origin of the solar wind in coronal funnels. To determine where the solar wind acceleration starts in funnels, we statistically evaluated the Doppler shift for regions with strong fields and vertical field lines. In the funnel shown in Fig. 5B, Si$^+$ has an average downflow speed of 2.0 ± 1.3 km/s at 4 Mm, C^{3+} an almost zero speed of 0.3 ± 3.3 km/s, and Ne^{7+} a clear upflow speed of 9.6 ± 2.0 km/s. Therefore, no outflow is found for the carbon and silicon ions. For calibration of the Doppler shift, we assumed that its average value is zero just above the solar limb (*36*).

To get firmer results on the flow velocity in the funnels, we calculated average Doppler shifts with data that were above the top 70% of the $|B_z|$ and Si II radiance. This Doppler-shift average indicates downflows of 0.3 km/s (with a σ of 2.8 km/s) for Si$^+$ and 0.5 km/s (σ = 3.2 km/s) for C^{3+}. As a result, when using Si$^+$ and C^{3+} as flow tracers, no significant solar wind outflow was found.

To compare the Doppler shift in the funnels with that in cell centers, we correlated the Si II, C IV, and Ne VIII Doppler shifts with $|B_z|$ and $|B_z/B|$, at 4.0 Mm, 4.5 Mm, and 20.6 Mm, respectively. It turned out that the downflow of Si$^+$ is influenced neither by $|B_z|$ nor by $|B_z/B|$. However, the Doppler shifts of C IV and Ne VIII and the Si II radiance are correlated with these parameters.

The results of the correlation analysis are given in Table 1. The data sets used are averages, derived from 31,321 original data points and obtained by forming 10 bins of $|B_z|$ or $|B_z/B|$. The critical correlation coefficient is 0.58 for a 95% confidence level. In Table 1, R is the correlation coefficient, and a and b are the parameters of the linear correlation $y = a + bx$. The condition of $|B_y/B_x| < 1$ was imposed to guarantee that the field is mainly in the x-z plane, in which case the LOS Doppler shift indicates vertical motions, because the horizontal magnetic field then has only an x component perpendicular to the LOS direction. Consequently, we largely exclude unwanted contributions resulting from Doppler shifts that are caused by horizontal plasma motion directed along the magnetic field. Similarly, the 39,117 points in the data set for Fig. 3B were selected with the requirement that $|B_z/B| > 0.5$, to eliminate data with mostly horizontal fields.

In Table 1, the fit coefficient b for C IV is positive. This indicates that downflow of C^{3+} ions may occur in regions with high $|B_z|$ and $|B_z/B|$ and, reversing the argument, that upflow can be expected for low values of $|B_z|$ and $|B_z/B|$. Consistent with supergranular motion, a slight trend appears for downflow near cell boundaries in contrast to upflow in cell

centers. No significant outflow can be identified for the C^{3+} ions in the funnels, but for the Ne^{7+} ions we clearly find outflow (together with weak radiance) within the funnels, where both $|B_z|$ and $|B_z/B|$ are large.

Three-dimensional source of the solar wind. Stimulated by our observations, we suggest a way to explain the origin of the fast solar wind. The transition region in CHs is full of magnetic loops of different sizes, mostly with heights of less than 5 Mm. Supergranular plasma convection in the photosphere keeps the feet of the loops moving and thus transfers kinetic energy to magnetic energy that is stored in the loops. They may finally move to a funnel region and undergo reconnection with existing open fields. Thereby, plasma previously confined in the loops is released, which may lead to both upflows and downflows. Ultimately, parts of the plasma contained in reconnecting loops are brought into the corona.

In the lower TR below about 5 Mm, we mainly have horizontal exchange of mass and energy between neighboring flux tubes, which is driven by supergranular motion. Above 5 Mm or higher, where reconnection between field lines of funnels and surrounding loops gradually ceases, vertical transport will become more important than horizontal, and the radial acceleration of the solar wind will actually start. Of course, the subsequent requirements on solar wind heating and acceleration are the same as in standard models.

This scenario is supported by the evidence provided in Fig. 3B, establishing a linear relation between the square root of the Si II radiance (as proxy of the plasma density ρ) and $|B_z|$, and by the observation in Fig. 4 that the highest Si II radiance is concentrated in the strong-field funnels. From magnetohydrodynamic theory we know that, for fields frozen in the plasma, the ratio B/ρ should be conserved (*37*), given that the flow velocity does not vary strongly along **B**. This is the case for horizontal plasma flow at 4 Mm, which is forced by magnetoconvection of a mainly vertical field. Thus, strong Si II emission may indicate mass concentrations caused by accumulation of advected magnetic flux.

Our scenario is akin to the magnetic furnace model proposed by Axford and McKenzie (*14–16*) and to ideas invoking reconnection of mesoscale loops (*38, 39*). We adopt from the furnace model the idea that reconnection plays a major role, as it will release plasma, set free magnetic energy, and produce Alfvén waves. However, our model of the nascent solar wind is intrinsically 3-D, and the magnetic field geometry is derived empirically. The plasma is accelerated in the funnel above a critical height of 5 Mm but originates below from the neighboring loops. The initial heating of the solar wind plasma is achieved in the side loops.

References and Notes

1. L. Biermann, *Zeitschrift für Astrophysik* **29**, 274 (1951).
2. E. N. Parker, *Astrophys. J.* **128**, 664 (1958).
3. M. Neugebauer, C. W. Snyder, *Science* **138**, 1095 (1962).
4. M. Neugebauer, C. W. Snyder, *J. Geophys. Res.* **71**, 4469 (1966).
5. Y. C. Whang, C. C. Chang, *J. Geophys. Res.* **70**, 4175 (1965).
6. R. E. Hartle, P. A. Sturrock, *Astrophys. J.* **151**, 1155 (1968).
7. A. J. Hundhausen, *Coronal Expansion and Solar Wind* (Springer-Verlag, Heidelberg, 1972).
8. E. Leer, T. E. Holzer, *Solar Phys.* **63**, 143 (1979).
9. E. Leer, T. E. Holzer, *J. Geophys. Res.* **85**, 4681 (1980).
10. C.-Y. Tu, *Solar Phys.* **109**, 149 (1987).
11. J. V. Hollweg, *J. Geophys. Res.* **91**, 4111 (1986).
12. V. H. Hansteen, E. Leer, *J. Geophys. Res.* **100**, 21577 (1995).
13. C.-Y. Tu, E. Marsch, *Solar Phys.* **171**, 363 (1997).
14. J. F. McKenzie, G. V. Sukhorukova, W. I. Axford, *Astron. Astrophys.* **330**, 1145 (1998).
15. W. I. Axford, J. F. McKenzie, in *Solar Wind Seven*, E. Marsch and R. Schwenn, Eds., (Pergamon Press, Oxford, 1992), pp. 1–5.
16. W. I. Axford, J. F. McKenzie, in *Cosmic Winds and the Heliosphere*, J. R. Jokipii, C. P. Sonett, M. S. Giampapa, Eds. (Arizona University Press, Tucson, 1997), pp. 31–66.
17. E. Marsch, C.-Y. Tu, *Solar Phys.* **176**, 87 (1997).
18. P. Hackenberg, E. Marsch, G. Mann, *Astron. Astrophys.* **360**, 1139 (2000).
19. A. H. Gabriel, *Philos. Trans. R. Soc.* **A281**, 339 (1976).
20. J. F. Dowdy Jr., A. G. Emslie, R. L. Moore, *Solar Phys.* **112**, 255 (1987).
21. K. Wilhelm *et al.*, *Solar Phys.* **170**, 75 (1997).
22. P. Lemaire *et al.*, *Solar Phys.* **170**, 105 (1997).
23. D. M. Hassler *et al.*, *Science* **283**, 810 (1999).
24. K. Wilhelm, I. E. Dammasch, E. Marsch, D. M. Hassler, *Astron. Astrophys.* **353**, 749 (2000).
25. L. D. Xia, E. Marsch, W. Curdt, *Astron. Astrophys.* **399**, L5 (2003).
26. L. D. Xia, E. Marsch, K. Wilhelm, *Astron. Astrophys.* **424**, 1025 (2004).
27. T. Wiegelmann, T. Neukirch, *Solar Phys.* **208**, 233 (2002).
28. P. H. Scherrer *et al.*, *Solar Phys.* **162**, 129 (1995).
29. E. Marsch, T. Wiegelmann, L. D. Xia, *Astron. Astrophys.* **428**, 629 (2004).
30. Ø. Lie-Svendsen, V. H. Hansteen, E. Leer, *Astrophys. J.* **596**, 621 (2003).
31. J. P. Delaboudinière *et al.*, *Solar Phys.* **162**, 291 (1995).
32. Materials and methods are available as supporting material on *Science* Online.
33. N. Seehafer, *Solar Phys.* **58**, 215 (1978).
34. H. Peter, *Astron. Astrophys.* **374**, 1108 (2001).
35. H. Peter, B. V. Gudiksen, Å. Nordlund, *Astrophys. J.* **617**, L85 (2004).
36. I. E. Dammasch, K. Wilhelm, W. Curdt, D. M. Hassler, *Astron. Astrophys.* **346**, 285 (1999).
37. T. J. M. Boyd and J. J. Sanderson, *Plasma Dynamics* (Thomas Nelson and Sons, London, 1969).
38. W. C. Feldman, B. L. Barraclough, J. L. Phillips, Y.-M. Wang, *Astron. Astrophys.* **316**, 355 (1996).
39. L. A. Fisk, *J. Geophys. Res.* **108**, 1157 (2003).
40. The National Natural Science Foundation of China supported C.-Y.T., C.Z., and L. Z. under projects with the contract nos. 40336053, 40174045 and 40436015; J.-X.Wang, contract no. 10233050; and L.-D.X., contract no. 40436015. The foundation Major Project of National Basic Research supported C.-Y.T., C.Z., L.-D.X., L. Z., and J.-X.W. under contract no. G-200078405. C.-Y.T. is supported by the Beijing Education Project XK100010404. The SUMER project is financially supported by DLR, CNES, NASA, and the ESA PRODEX program (Swiss contribution). SUMER, EIT, and MDI are instruments on SOHO, an ESA and NASA mission. We thank the teams of MDI and EIT for providing the magnetic field data and the context image.

Causal Protein-Signaling Networks Derived from Multiparameter Single-Cell Data

Karen Sachs,[1]* Omar Perez,[2]* Dana Pe'er,[3]* Douglas A. Lauffenburger,[1]† Garry P. Nolan[2]†

Machine learning was applied for the automated derivation of causal influences in cellular signaling networks. This derivation relied on the simultaneous measurement of multiple phosphorylated protein and phospholipid components in thousands of individual primary human immune system cells. Perturbing these cells with molecular interventions drove the ordering of connections between pathway components, wherein Bayesian network computational methods automatically elucidated most of the traditionally reported signaling relationships and predicted novel interpathway network causalities, which we verified experimentally. Reconstruction of network models from physiologically relevant primary single cells might be applied to understanding native-state tissue signaling biology, complex drug actions, and dysfunctional signaling in diseased cells.

Extracellular cues trigger a cascade of information flow, in which signaling molecules become chemically, physically, or locationally modified; gain new functional capabilities; and affect subsequent molecules in the cascade, culminating in a phenotypic cellular response. Mapping of signaling pathways typically has involved intuitive inferences arising from the aggregation of studies of individual pathway components from diverse experimental systems. Although pathways are often conceptualized as distinct entities responding to specific triggers, it is now understood that interpathway cross-talk and other properties of networks reflect underlying complexities that cannot be explained by the consideration of individual pathways or model systems in isolation. To properly understand normal cellular responses and their potential disregulation in disease, a global multivariate approach is required (*1*). Bayesian networks (*2*), a form of graphical models, have been proffered as a promising framework for modeling complex systems such as cell signaling cascades, because they can represent probabilistic dependence relationships among multiple interacting components (*3–5*). Bayesian network models illustrate the effects of pathway components on each other (that is, the dependence of each biomolecule in the pathway on other biomolecules) in the form of an influence diagram. These models can be automatically derived from experimental data through a statistically founded computational procedure termed network inference. Although the relationships are statistical in nature, they can sometimes be interpreted as causal influence connections when interventional data are used; for example, with the use of kinase-specific inhibitors (*6, 7*).

There are several attractive properties of Bayesian networks for the inference of signaling pathways from biological data sets. Bayesian networks can represent complex stochastic nonlinear relationships among multiple interacting molecules, and their probabilistic nature can accommodate noise that is inherent to biologically derived data. They can describe direct molecular interactions as well as indirect influences that proceed through additional unobserved components, a property crucial for discovering previously unknown effects and unknown components. Therefore, very complex relationships that likely exist in

[1]Biological Engineering Division, Massachusetts Institute of Technology (MIT), Cambridge, MA 02139, USA. [2]Stanford University School of Medicine, The Baxter Laboratory of Genetic Pharmacology, Department of Microbiology and Immunology, Stanford, CA 94305, USA. [3]Harvard Medical School, Department of Genetics, Boston, MA 02115, USA.

*These authors contributed equally to this work.
†To whom correspondence should be addressed. E-mail: lauffen@mit.edu (D.A.L.); gnolan@stanford.edu (G.P.N.)